

Saturation and self-absorption effects in the angle-dependent $2p3d$ resonant inelastic X-ray scattering spectra of Co^{3+} Ru-Pan Wang,^a Hebatalla Elnaggar,^a Charles J. Titus,^b Keisuke Tomiyasu,^{c,d} Jaap Geessinck,^e Gertjan Koster,^e Federica Frati,^a Jun Okamoto,^f Di-Jing Huang^f and Frank M. F. de Groot^{a*}

Received 5 March 2020

Accepted 12 April 2020

Edited by K. Kvashnina, ESRF – The European Synchrotron, France

Keywords: angle-dependent RIXS/RXES; saturation and self-absorption effects.

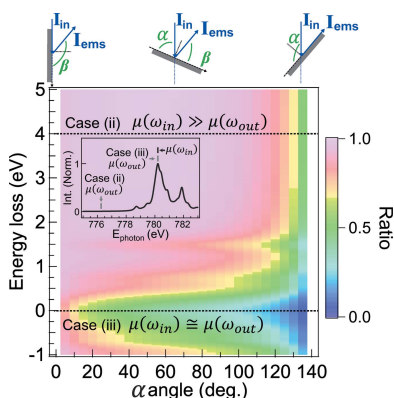
^aDebye Institute for Nanomaterials Science, Utrecht University, Universiteitsweg 99, 3584 CG Utrecht, The Netherlands, ^bDepartment of Physics, Stanford University, Stanford, CA 94305, USA, ^cDepartment of Physics, Tohoku University, Aoba, Sendai 980-8578, Japan, ^dNISSAN ARC Ltd, 1 Natsushima-cho, Yokosuka, Kanagawa 237-0061, Japan, ^eMESA+ Institute for Nanotechnology, University of Twente, 7500 AE Enschede, The Netherlands, and ^fCondensed Matter Physics Group, National Synchrotron Radiation Research Center, 101 Hsin-Ann Road, Hsinchu Science Park, Hsinchu 30076, Taiwan, Republic of China. *Correspondence e-mail: f.m.f.degroot@uu.nl

Angle-dependent $2p3d$ resonant inelastic X-ray scattering spectra of a LaCoO_3 single crystal and a 55 nm LaCoO_3 film on a SrTiO_3 substrate are presented. Theoretical calculation shows that, with ~ 20 meV resolved Co $2p3d$ resonant inelastic X-ray scattering (RIXS), the excited states of the isotropic $^1A_{1g}(O_h)$ ground state are split by $3d$ spin–orbit coupling, which can be distinguished via their angular dependence. However, strong self-absorption and saturation effects distort the spectra of the LaCoO_3 single crystal and limit the observation of small angular dependence. In contrast, the RIXS on 55 nm LaCoO_3 shows less self-absorption effects and preserves the angular dependence of the excited states.

1. Introduction

Resonant inelastic X-ray scattering (RIXS) is a developing technique that is used to investigate the ground and excited states of transition metals, in particular when combined with the angular degrees of freedom (*i.e.* angle-dependent measurements). The angular dependence of RIXS has been examined by Michel van Veenendaal using crystal field calculations for L - and M -edges in the case of a single valence hole (or equally a single electron) (van Veenendaal, 2006). Based on these calculations, one is able to discriminate between different transitions of the d -states via their spin characteristics using certain photon polarizations or experimental geometries for RIXS (van Veenendaal, 2006; Moretti Sala *et al.*, 2011). By including the spin–orbit coupling, exchange field ($2J_{\text{ex}}$) or external magnetic field, the system symmetry is further reduced (van Schooneveld *et al.*, 2012). This implies that RIXS can even have the sensitivity to investigate the fine structure of spin–orbit coupling in multi-electron systems. However, this sensitivity is commonly hampered by geometrical aspects of the experiment.

The RIXS cross-section can be explained as a combination of an absorption (*photon-in*) process and an emission (*photon-out*) process. The absorption process excites the electrons to higher energy levels and the emission process emits photons when the electrons decay to the lower energy levels. Two geometrical effects have to be taken into account here: (i) the probing depth is dependent on the X-ray absorption spectroscopy (XAS) cross-section (saturation) and (ii) the emitted



photons can be re-absorbed (self-absorption). Consequently, the emission intensity might be distorted according to the photon energy and the experimental geometry, which is well known in fluorescence yield XAS (FY-XAS) (Jaklevic *et al.*, 1977; Zschech *et al.*, 1992; Tröger *et al.*, 1992; Eisebitt *et al.*, 1993; Chakarian *et al.*, 1998; Nakajima *et al.*, 1999; Achkar *et al.*, 2011). As such, it also distorts the RIXS spectra (Chabot-Couture *et al.*, 2010; Dallera *et al.*, 1997).

In this article, we raise awareness that the $2p3d$ RIXS intensity is distorted not only by the incident-energy-dependent saturation but also by emission-energy-dependent self-absorption. A model is proposed to describe the angle-dependent coefficients of the RIXS intensity for the saturation and self-absorption effects, which has been used to correct the $2p3d$ RIXS intensity of magnons in cuprate (Minola *et al.*, 2015), where we applied the self-absorption-added coefficients to generate a theoretical prediction. The angle-dependent $2p3d$ RIXS of a LaCoO₃ single crystal and a 55 nm LaCoO₃ film on an SrTiO₃ substrate (LaCoO₃/SrTiO₃ film) were compared to illustrate these effects. Furthermore, we show that the fine structure of the spin–orbit coupling and exchange interaction within the $3d^6$ manifold of a Co³⁺ ion can potentially be revealed using RIXS angle-dependent measurements.

2. Theory

2.1. Kramers–Heisenberg formula

The RIXS cross-section is determined by the Kramers–Heisenberg equation (Kramers & Heisenberg, 1925),

$$F_{\text{RIXS}}(\omega_{\text{in}}, \omega_{\text{out}}) = r_c^2 \frac{\omega_{\text{out}}}{\omega_{\text{in}}} \sum_f |A_f(\omega_{\text{in}})|^2 \times \delta(\hbar\omega_{\text{in}} + E_g - \hbar\omega_{\text{out}} - E_f), \quad (1)$$

where $A_f(\omega_{\text{in}})$ is the scattering amplitude which is defined as

$$A_f(\omega_{\text{in}}) = \sum_m \frac{\langle f|V_E|m\rangle\langle m|V_I|g\rangle}{\hbar\omega_{\text{in}} + E_g - E_m + i\Gamma} = \langle f|V_E G(\omega_{\text{in}})V_I|g\rangle. \quad (2)$$

Here $\hbar\omega_{\text{in}}$ and $\hbar\omega_{\text{out}}$ are the energies of the incident and the emitted photons; E_g , E_f and E_m are the eigenvalues of the ground state $|g\rangle$, the final state $|f\rangle$ and the intermediate state $|m\rangle$, respectively; Γ gives the lifetime broadening of the intermediate state. $V_I(V_E)$ is the transition operator induced by the electro-magnetic field of the incident (emitted) photon and can be expanded as $\boldsymbol{\varepsilon}_I \cdot \hat{P}_I \exp(i\mathbf{k}_I \cdot \mathbf{r}_I)$ ($\boldsymbol{\varepsilon}_E \cdot \hat{P}_E \exp(i\mathbf{k}_E \cdot \mathbf{r}_E)$). $\boldsymbol{\varepsilon}_I$ ($\boldsymbol{\varepsilon}_E$) and \hat{P}_I (\hat{P}_E) describe the electric field polarization vector and the momentum operator of the incident(emitted) photon. \mathbf{k}_I (\mathbf{k}_E) and \mathbf{r}_I (\mathbf{r}_E) give the wave-vector and position of the electro-magnetic wave. For $2p3d$ RIXS, the $2p3d$ ($3d2p$) transition operator is approximated as an electric dipole operator $\boldsymbol{\varepsilon}_I \cdot \hat{P}_I$ ($\boldsymbol{\varepsilon}_E \cdot \hat{P}_E$) for the absorbed (emitted) channel, *i.e.* $\exp(i\mathbf{k}_I \cdot \mathbf{r}_I)[\exp(i\mathbf{k}_E \cdot \mathbf{r}_E)] \simeq 1$. The scattering amplitude can also be described by Green's function [$G(\omega_{\text{in}}) = \sum_m (\hbar\omega_{\text{in}} - E_m + i\Gamma)^{-1}$], where the ground-state energy (E_g) is taken as zero. Note that we can ignore the

scattering coefficient $r_c^2(\omega_{\text{out}}/\omega_{\text{in}})$ because $(\omega_{\text{out}}/\omega_{\text{in}}) \simeq 1$ ($\omega_{\text{in}} \simeq \omega_{\text{out}}$) and the classical electron radius r_c is constant.

For a better insight into the angular dependence of RIXS, many authors have already reformulated the scattering amplitude by using the spherical tensor expansion (Luo *et al.*, 1993; van Veenendaal, 2006; Juhin *et al.*, 2014; Moretti Sala *et al.*, 2011). In the case of the $2p3d$ RIXS within the fast-collision approximation, the interference of the intermediate states can be ignored and Green's function can be simplified by $G^\pm(\omega_{\text{in}}) = (\hbar\omega_{\text{in}} - \bar{E}_{j^\pm} + i\Gamma)^{-1}$, where \bar{E}_{j^\pm} is the mean energy for the spin–orbit coupled $2p_{3/2}$ and $2p_{1/2}$ edges (Luo *et al.*, 1993; van Veenendaal, 2006). Then the $2p3d$ RIXS cross-section formula can be expanded as

$$A_f^\pm(\omega_{\text{in}}) = P_{\text{dipole}}^2 \sum_{Q=0}^2 \sum_{q=-Q}^Q G^\pm(\omega_{\text{in}}) T_{Qq}^*(\varepsilon_E, \varepsilon_I) \langle f|W_{Qq}^\pm|g\rangle. \quad (3)$$

Van Veenendaal pointed out that the cross-section is now described by the effective dd transition operators W_{Qq} from a $3d^n$ ground state to another $3d^n$ final state with a polarization weighting factor $T_{Qq}(\varepsilon_E, \varepsilon_I)$ (van Veenendaal, 2006). W_{Qq} is a one-particle operator which is constructed by the orbital- and spin-dependent tensors. The system geometry [Fig. 1(a)] is reflected by the polarization tensors $T_{Qq}(\varepsilon_E, \varepsilon_I)$. P_{dipole} is the reduced matrix element between the $2p$ (core) and $3d$ (valence) levels. With this simplification, the beam polarization and the electronic configuration can be decoupled from each other and they therefore can be linked directly to the experimental geometry.

In this work, the ground and excited states' energies and the $2p3d$ RIXS spectra were computed using the program *Quanty*, where both the tetragonal distortion and ligand-to-metal charge transfer could be considered (Haverkort *et al.*, 2012; de Groot, 2005). The polarization operators were expanded on

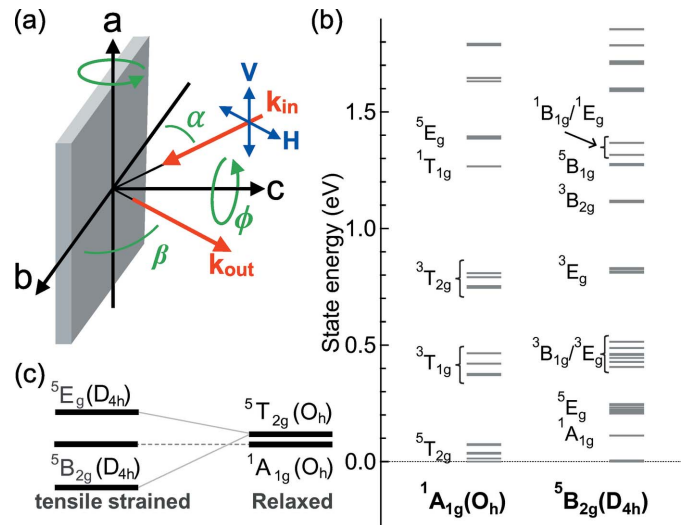


Figure 1 (a) Illustration of the geometry and the angles. (b) Energy diagram for the $1A_{1g}(O_h)$ ground state and the $5B_{2g}(D_{4h})$ ground state. (c) The $5B_{2g}(D_{4h})$ state is the split subgroup of the $3T_{2g}(O_h)$ state in the tetragonal distortion (in-plane tensile strained) (Wang *et al.*, 2019).

the coordinates of the crystal field operator, where the axes are given by **a**, **b** and **c** as indicated in Fig. 1(a). Because no polarization analyzer was used, unpolarized emitted photons have been assumed and were composed by the summation of two orthogonal linear polarized beams (Juhin *et al.*, 2014). The energy diagrams of the final (excited) states $|f\rangle$ were obtained from the cluster calculation using the program *Quanty* (Haverkort, 2010). The exchange interaction is estimated to be 6 meV ($T_c \simeq 70$ K) which is neglected in the current simulation and discussion since it shows only tiny effects on the spectra. The electronic configurations of Co^{3+} ions in the LaCoO_3 crystal and the $\text{LaCoO}_3/\text{SrTiO}_3$ film were suggested to be the pure $^1A_{1g}(\text{O}_h)$ configuration and a mixture of the $^1A_{1g}(\text{O}_h)$ and the $^5B_{2g}(\text{D}_{4h})$ configurations, respectively (Tomiyasu *et al.*, 2017; Wang *et al.*, 2019). The model parameters of the $^1A_{1g}(\text{O}_h)$ ground state configuration are: $F_{dd}^2 = 9.371$ eV, $F_{dd}^4 = 5.859$ eV, $\zeta_d = 0.055$ eV, $10Dq = 0.595$ eV, $U = 6.5$ eV, $Q = 7.5$ eV, $\Delta = 1.5$ eV, $T_{t_{2g}} = 1.8$ eV and $T_{e_g} = 3.118$ eV. For the $^5B_{2g}(\text{D}_{4h})$ ground state configuration, $D_S = -0.12$ eV and $D_t = -0.018$ eV are applied in addition to the $^1A_{1g}(\text{O}_h)$ case. The calculated excited states are indicated by the term symbol notations in Fig. 1(b). We note that the $^5B_{2g}(\text{D}_{4h})$ state is the subgroup of the $^5T_{2g}(\text{O}_h)$ state in the tetragonal distortion [Fig. 1(c)].

2.2. Saturation and self-absorption effects

To simulate the saturation and the self-absorption effects, the transmitted photons (I_T) within a small distance $d\ell$ can be described by the differential Lambert–Beer relation with the absorption factor of the incident beam $\mu(\omega_{\text{in}})$,

$$dI_T = -\mu(\omega_{\text{in}}) I_0 d\ell. \quad (4)$$

The integration of equation (4) from zero to the path length ℓ becomes:

$$I_T(\ell) = I_0 \exp[-\mu(\omega_{\text{in}}) \ell]. \quad (5)$$

Here the constant I_0 gives the finite incoming photon flux. We note that this relation also depends on the surface profile of the sample. For a flat sample, the absorption probing depth d depends on the angle α between the incident photon and the sample surface [Fig. 2(a)], which gives the relation $\ell = d/\sin \alpha$. Thus we can rewrite equation (5) as a function of d ,

$$I_T(d) = I_0 \exp\left[-\mu(\omega_{\text{in}}) \frac{d}{\sin \alpha}\right]. \quad (6)$$

For the emission process, the total emitted flux is the integration of the beam of emitted photons from the surface to the probing depth d . This implies the path length $\ell' = d/\sin \beta$, where β is the angle between the scattered beam and sample surface [Fig. 2(a)]. Then the total emitted flux becomes

$$I_{\text{ems}}(d) = \int_{z=0}^{z=d} dI_S(z) \exp\left[-\mu(\omega_{\text{out}}) \frac{z}{\sin \beta}\right]. \quad (7)$$

Here, $dI_S(z)$ stands for the scattering possibility per absorbed photon within a finite distance dz at a certain depth z , from

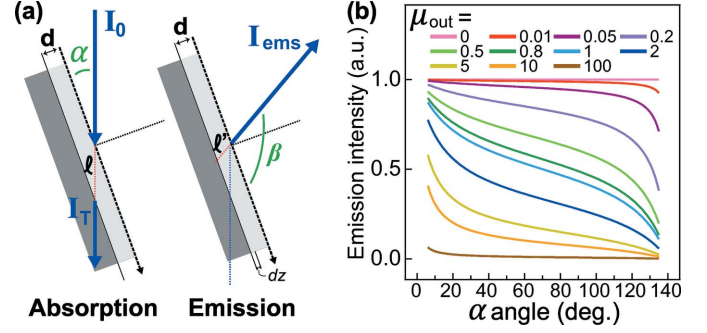


Figure 2

(a) Illustration of the geometry for the absorption and emission process. (b) Self-absorption-added coefficients $\{1/[\mu(\omega_{\text{in}}) + \mu(\omega_{\text{out}})(\sin \alpha / \sin \beta)]\}$ as a function of the sample rotation angle α , where $\mu(\omega_{\text{in}}) = 1$ and $\mu(\omega_{\text{out}})$ is scaled from zero to infinity to simulate the trends. The scattering angle ($\alpha + \beta$) is set to 140° .

which we can expand $dI_S(z)$ into equation (4) with a scattering possibility $S(\omega_{\text{in}}, \omega_{\text{out}})$ as

$$\begin{aligned} dI_S(z) &= S(\omega_{\text{in}}, \omega_{\text{out}}) dI_T \\ &= S(\omega_{\text{in}}, \omega_{\text{out}}) \mu(\omega_{\text{in}}) I_T(z) \frac{dz}{\sin \alpha}. \end{aligned} \quad (8)$$

The scattering possibility $S(\omega_{\text{in}}, \omega_{\text{out}})$ is determined by the state transition possibility. To a good approximation, the multiplication $S(\omega_{\text{in}}, \omega_{\text{out}}) \mu(\omega_{\text{in}})$ represents the scattering intensity of RIXS. We note that our simulation calculated the scattering intensity of RIXS including the interference effects. In addition, the Auger decay channels are also state dependent. This will induce additional scaling factors on the emission intensity. In the case of the $2p3d$ channels, the energy dependence in Auger decay is less than 10% (de Groot *et al.*, 1994) and we approximate them as constant. By integrating equation (7), the emission intensity including both the saturation and the self-absorption effects is written as (as a function of probing depth d)

$$\begin{aligned} I_{\text{ems}}(d) &= \int_{z=0}^{z=d} I_0 S(\omega_{\text{in}}, \omega_{\text{out}}) \mu(\omega_{\text{in}}) \exp\left[-\mu(\omega_{\text{in}}) \frac{z}{\sin \alpha}\right] \\ &\quad \times \frac{dz}{\sin \alpha} \exp\left[-\mu(\omega_{\text{out}}) \frac{z}{\sin \beta}\right] \\ &= I_0 \frac{S(\omega_{\text{in}}, \omega_{\text{out}}) \mu(\omega_{\text{in}})}{\sin \alpha} \frac{1}{[\mu(\omega_{\text{in}})/\sin \alpha] + [\mu(\omega_{\text{out}})/\sin \beta]} \\ &\quad \times \left(1 - \exp\left\{-d \left[\frac{\mu(\omega_{\text{in}})}{\sin \alpha} + \frac{\mu(\omega_{\text{out}})}{\sin \beta}\right]\right\}\right). \end{aligned} \quad (9)$$

This equation has already been discussed for the cases of FY-XAS spectra (Jaklevic *et al.*, 1977; Zschech *et al.*, 1992; Tröger *et al.*, 1992; Eisebitt *et al.*, 1993; Chakarian *et al.*, 1998; Nakajima *et al.*, 1999; Achkar *et al.*, 2011; Chabot-Couture *et al.*, 2010) by assuming that $\mu(\omega_{\text{out}})$ is approximately constant. The spectral saturation is described by the term $\mu(\omega_{\text{in}})/\sin \alpha$ and is sensitive to the incidence angle α ; the self-absorption effect is determined by the emission angle β . For RIXS, however, $\mu(\omega_{\text{out}})$ cannot be treated as a constant because the emitted photon energy is analyzed.

2.2.1. Thin samples. If the sample thickness (D) is much smaller than the attenuation length (η), *i.e.* $\eta \gg D \simeq d \rightarrow 0$, we can use the approximation of the exponential function, $\exp(-x) \simeq 1 - x$. Then we obtain

$$I_{\text{ems}}(D \rightarrow 0) \simeq I_0 \mu(\omega_{\text{in}}) S(\omega_{\text{in}}, \omega_{\text{out}}) \frac{D}{\sin \alpha}. \quad (10)$$

Equation (10) shows that the emission intensity is proportional to the incoming photon flux I_0 , the absorption factor of the incident beam $\mu(\omega_{\text{in}})$, the scattering factor $S(\omega_{\text{in}}, \omega_{\text{out}})$, the sample thickness D and the angle α . Thus, the total emission intensity only depends on the rotation angle α , which changes the overall intensity as a function of angle but shows no energy-dependent spectral distortion caused by the self-absorption effect. This self-absorption-free approximation is also applied to dilute specimens. $\mu(\omega_{\text{in}})$ and $\mu(\omega_{\text{out}})$ are the total absorption factors at certain energies ω_{in} and ω_{out} , which can also be described by the summation over all individual elements 'X', *i.e.* $\mu(\omega) = \sum_X \mu_X(\omega)$ and $S(\omega_{\text{in}}, \omega_{\text{out}}) = \sum_X S_X(\omega_{\text{in}}, \omega_{\text{out}})$. The FY-XAS or RIXS intensity is proportional to the multiplication $S(\omega_{\text{in}}, \omega_{\text{out}}) \mu(\omega_{\text{in}})$. By ignoring the inter-atom interaction, this multiplication of the two summation factors $\mu(\omega)S(\omega_{\text{in}}, \omega_{\text{out}})$ is replaced by the summation of the multiplications $\sum_X \mu_X(\omega) S_X(\omega_{\text{in}}, \omega_{\text{out}})$. Then equation (10) is expressed as

$$I_{\text{ems}}(D \rightarrow 0) = I_0 \sum_X \mu_X(\omega_{\text{in}}) S_X(\omega_{\text{in}}, \omega_{\text{out}}) \frac{D}{\sin \alpha}. \quad (11)$$

In the case of the Co L_3 edge, the absorption factor and scattering possibility of the other elements are constant so that equation (11) becomes

$$I_{\text{ems}}(D) = I_0 [\mu_{\text{Co}}(\omega_{\text{in}}) S_{\text{Co}}(\omega_{\text{in}}, \omega_{\text{out}}) + \text{constant}] \frac{D}{\sin \alpha}. \quad (12)$$

The state-dependent scattering possibility $S_{\text{Co}}(\omega_{\text{in}}, \omega_{\text{out}})$ implies that the partial fluorescence yield X-ray absorption is not identical to the normal absorption. Liu *et al.* show good agreement of such state-dependent behavior between experimental and calculated results in dilute specimens (Liu *et al.*, 2018). If $S_{\text{Co}}(\omega_{\text{in}}, \omega_{\text{out}})$ is approximated as a constant, the scattered spectrum is equivalent to the normal absorption $\mu_{\text{Co}}(\omega_{\text{in}})$.

2.2.2. Thick samples. If the sample is thick (large D), d becomes infinity; the incident photons are fully absorbed. Thus the exponential term in equation (9) becomes zero. Then we obtain the scattering intensity as a function of the photon energy and sample geometry,

$$\begin{aligned} I_{\text{ems}}(d \rightarrow \infty) & \quad (13) \\ &= I_0 \sum_X \frac{S_X(\omega_{\text{in}}, \omega_{\text{out}}) \mu_X(\omega_{\text{in}})}{\sin \alpha} \frac{1}{[\mu(\omega_{\text{in}})/\sin \alpha] + [\mu(\omega_{\text{out}})/\sin \beta]} \\ &= I_0 \sum_X S_X(\omega_{\text{in}}, \omega_{\text{out}}) \mu_X(\omega_{\text{in}}) \frac{1}{\mu(\omega_{\text{in}}) + \mu(\omega_{\text{out}})(\sin \alpha / \sin \beta)}. \end{aligned}$$

This relation has been applied to a method of inverse partial fluorescence yield to obtain bulk-sensitive absorption spectra (Achkar *et al.*, 2011), where the key aspect of inverse partial

fluorescence yield is that one applies the partial fluorescence yield away from the target edges, so that the multiplication of $\mu_X(\omega_{\text{in}})$ and $S_X(\omega_{\text{in}}, \omega_{\text{out}})$ is approximately constant. For example, in CoO, the element cobalt and the element oxygen are considered. Then the emission intensity becomes

$$I_{\text{ems}} = I_0 \frac{S_{\text{Co}}(\omega_{\text{in}}, \omega_{\text{out}}) \mu_{\text{Co}}(\omega_{\text{in}}) + S_{\text{O}}(\omega_{\text{in}}, \omega_{\text{out}}) \mu_{\text{O}}(\omega_{\text{in}})}{\mu_{\text{Co}}(\omega_{\text{in}}) + \mu_{\text{O}}(\omega_{\text{in}}) + [\mu_{\text{Co}}(\omega_{\text{out}}) + \mu_{\text{O}}(\omega_{\text{out}})] \frac{\sin \alpha}{\sin \beta}}. \quad (14)$$

When accumulating the oxygen K edge fluorescence signal, the emission intensity of cobalt is negligible [$\mu_{\text{Co}}(\omega_{\text{in}}) S_{\text{Co}}(\omega_{\text{in}}, \omega_{\text{out}}) \simeq 0$]. The emission spectrum becomes the summation of the emitted photon energy (ω_{out}) at the oxygen K edge, which leads to $\mu_{\text{O}}(\omega_{\text{in}}) S_{\text{O}}(\omega_{\text{in}}, \omega_{\text{out}})$ that is approximated as constant with respect to the incident energy of the cobalt $L_{2,3}$ edge. It also implies that the absorption factors of the emitted photons [$\mu_{\text{Co}}(\omega_{\text{out}})$ and $\mu_{\text{O}}(\omega_{\text{out}})$] are approximately constant. Then the emission intensity is simplified as

$$I_{\text{ems}} = I_0 \frac{C_1}{\mu_{\text{Co}}(\omega_{\text{in}}) + \mu_{\text{O}}(\omega_{\text{in}}) + C_2}. \quad (15)$$

The inverse intensity becomes $I_{\text{ems}}^{-1} \propto \mu_{\text{Co}}(\omega_{\text{in}}) + \mu_{\text{O}}(\omega_{\text{in}}) + C_2$, where C_1 , C_2 and $\mu_{\text{O}}(\omega_{\text{in}})$ are constant with respect to the incident energy of the cobalt $L_{2,3}$ edge. Thus the emission intensity is mainly dominated by the absorption factor $\mu_{\text{Co}}(\omega_{\text{in}})$ which provides a bulk-sensitive absorption spectrum free from self-absorption and saturation effects.

For RIXS, equation (13) shows that the scattering intensity of RIXS should be multiplied by the self-absorption-added coefficients $1/[\mu(\omega_{\text{in}}) + \mu(\omega_{\text{out}})(\sin \alpha / \sin \beta)]$ when saturation and self-absorption effects are included (Chabot-Couture *et al.*, 2010). Fig. 2(b) shows this saturation relation as a function of α . Here, $\mu(\omega_{\text{in}})$ is fixed at one and $\mu(\omega_{\text{out}})$ is scaled from zero to a hundred (infinity) to simulate the trends. The scattering angle is 140° . Depending on the competition between $\mu(\omega_{\text{in}})$ and $\mu(\omega_{\text{out}})$, three cases can occur:

(i) $\mu(\omega_{\text{out}}) \gg \mu(\omega_{\text{in}})$ ($I_{\text{ems}} \simeq 0$). In this condition, the absorption factor of the emitted photons is much bigger than the incident beam absorption. The scattered photons can more easily be reabsorbed in the emission process, which implies that the emission intensity tends to vanish [the line $\mu(\omega_{\text{out}}) \simeq 100$ in Fig. 2(b)].

(ii) $\mu(\omega_{\text{out}}) \ll \mu(\omega_{\text{in}})$ ($I_{\text{ems}} \simeq I_0 \{ [S_X(\omega_{\text{in}}, \omega_{\text{out}}) \mu_X(\omega_{\text{in}})] / \mu(\omega_{\text{in}}) \}$). When the absorption factor of the emission beam is much smaller than the incident beam, the angle-dependent term is negligible together with the small $\mu(\omega_{\text{out}})$ value. In other words, the spectrum distortion is angle-independent [the line $\mu(\omega_{\text{out}}) \simeq 0$ in Fig. 2(b)].

(iii) $\mu(\omega_{\text{out}}) \simeq \mu(\omega_{\text{in}})$. In this case, none of the factors can be omitted, as shown by the lines $\mu(\omega_{\text{out}}) \simeq 1$. The self-absorption effect is dependent on the geometry and the photon energy of both the incident and emitted beams. From the equation, we specify the two extreme conditions. The first case is that the incident beam is propagating along the sample surface plane (grazing incidence), where $\alpha \simeq 0$. Here, the

emission intensity $I_{\text{ems}} \simeq I_0 \{ [S_X(\omega_{\text{in}}, \omega_{\text{out}}) \mu_X(\omega_{\text{in}})] / \mu(\omega_{\text{in}}) \}$ provides a maximum value. But the absorption cross-section is saturated due to the competition between the absorption factor on certain element $\mu_X(\omega_{\text{in}})$ and the total absorption factor $\mu(\omega_{\text{in}})$. The second case describes the propagation of the emitted beam being along the sample surface plane (grazing exit). It implies that the scattered photons are totally reabsorbed and no scattering intensity should be expected ($I_{\text{ems}} \simeq 0$).

We present in Fig. 3 the influence of the self-absorption and saturation effects on the low-spin $\text{Co}^{3+} 1A_{1g}(O_h)$ ground state as an example for bulk LaCoO_3 . The theoretical $\mu_{\text{Co}}(\omega_{\text{out}})$ and $\mu_{\text{Co}}(\omega_{\text{in}})$ can be obtained by calculating the XAS spectra. $\mu_{\text{Co}}(\omega_{\text{out}})$ is approximately equal to the total $\mu_{\text{Co}}(\omega)$. For a fixed incident photon energy, the incident absorption factor $\mu_{\text{Co}}(\omega_{\text{in}})$ is always the same. Note that the total $\mu(\omega)$ includes not only the contribution of the target element but also the contributions from other elements. We assume that the other absorption channels result in a constant background μ_B of about 5% of the total $\mu(\omega)$ (the value is estimated in Appendix A). Fig. 3 shows the self-absorption-added coefficients $\{1/[\mu(\omega_{\text{in}}) + \mu(\omega_{\text{out}})(\sin \alpha / \sin \beta)]\}$ as a function of rotation angle and energy loss (energy transfer). The emitted signal can be classified into two parts: the dd excitations and the fluorescence. The emitted photons' energies of dd excitations are close to the L_3 edge absorption, which implies that $\mu(\omega_{\text{out}}^{dd}) \simeq \mu(\omega_{\text{in}})$, so case (iii) is applied. In contrast, the emission energy of the fluorescence feature is ~ 2.5 eV lower than the elastic peak for the main line of L_3 RIXS, so it experiences considerably less absorption. According to the

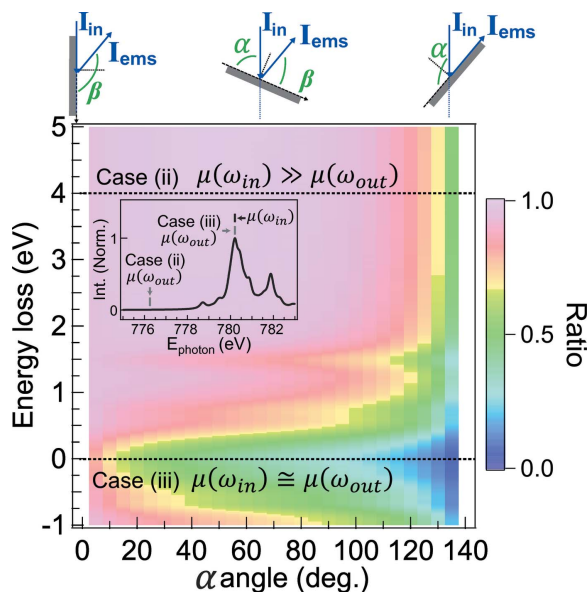


Figure 3
The self-absorption-added coefficients $\{1/[\mu(\omega_{\text{in}}) + \mu(\omega_{\text{out}})(\sin \alpha / \sin \beta)]\}$ as a function of rotation angle and emitted photon energy loss for a low-spin $\text{Co}^{3+} 1A_{1g}(O_h)$ ground state, where $\alpha + \beta = 140^\circ$. The absorption factor μ is plotted in the inset. It indicates also the conditions of case (ii) $\mu(\omega_{\text{in}}) \gg \mu(\omega_{\text{out}})$ and case (iii) $\mu(\omega_{\text{in}}) \simeq \mu(\omega_{\text{out}})$. We note that the absorption factor has been normalized to the maximum and the self-absorption-added coefficients have been normalized to the maximum of the region of interest.

calculation, the absorption factor 2.5 eV before the edge is considerably smaller. We can assume that $\mu(\omega_{\text{out}}^F) \ll \mu(\omega_{\text{in}})$ which leads to case (ii) and shows no angular dependence. This shows that the overall intensity of the angle-dependent spectra can be normalized to the fluorescence feature.

3. Methodology

The single crystal of LaCoO_3 was prepared from the polycrystalline sample which was a stoichiometric mixture of high-purity powders of La_2O_3 and Co_3O_4 using the floating-zone method. The $\text{LaCoO}_3/\text{SrTiO}_3$ thin film was fabricated using pulsed laser deposition in combination with *in situ* reflection high-energy electron diffraction (RHEED). It was grown under a 0.2 mbar O_2 background pressure and at a deposition temperature of 750°C . The laser flux was adjusted to 1.9 J cm^{-2} . The sample thickness was 55 nm which is determined by X-ray reflectivity (XRR) measurement. More sample details are given by Tomiyasu *et al.* (2017) and Wang *et al.* (2019).

The Co $2p3d$ RIXS measurements were performed at beamline BL05A1 at the Taiwan Light Source (Lai *et al.*, 2014). The scattering angle ($\alpha + \beta$) was set at 140° for the LaCoO_3 single crystal and at 90° for the $\text{LaCoO}_3/\text{SrTiO}_3$ film. Both samples were measured at the Co L_3 edge (~ 780 eV) at 20 K. The experimental resolution of RIXS was calibrated as ~ 90 meV and the recorded incident energy broadening was ~ 1000 meV (FWHM). The calculations of $2p3d$ RIXS spectra were performed using the program *Quanty* with intrinsic lifetime broadenings of ~ 300 meV and 20 meV (FWHM) for the intermediate and final states, respectively (Haverkort *et al.*, 2012). In addition to the intrinsic lifetime broadening, we applied 1000 meV and 60 meV Gaussian broadening to simulate the experiment incident energy window and the energy loss resolution. However, the self-absorption effect depends on the intrinsic absorption factor (μ), which is independent of the instrumental broadening. Thus, the self-absorption-added coefficients in Fig. 3 include only intrinsic lifetime broadening. The experimental spectra were normalized to the fluorescence feature, where the fluorescence feature was subtracted from the normalized spectra (see also Appendix B). The simulations were normalized to the charge transfer features.

4. Results and discussion

Fig. 4(a) shows the angle-dependent RIXS of the LaCoO_3 single crystal at the maximum of the Co L_3 edge. The elastic peak shows a maximum intensity at the specular angle ($\beta = \alpha$) due to strong reflection. In contrast, the intensity of the dd excitations decreases when α increases. In comparison, we show in Fig. 4(b) the α -dependent calculation of the $1A_{1g}(O_h)$ ground state, where the angular dependence can be observed. The $3T_{1g}(O_h)$ state slightly changes its intensity and shifts its position due to the competition of spin-orbit fine structures, which will be discussed later. However, the trends are not in good agreement with the experimental results because the

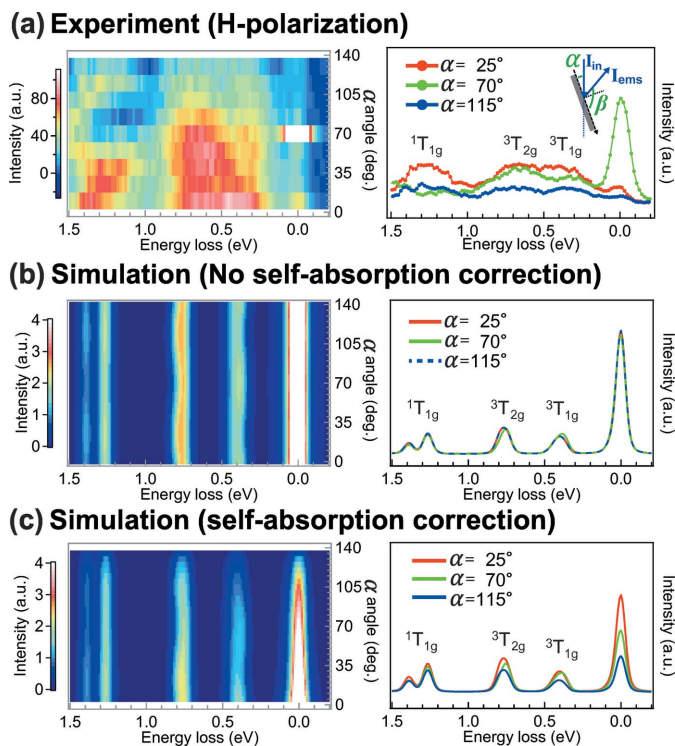


Figure 4
The $2p3d$ RIXS results as a function of rotation angle α (left panels) and slice cuts (right panels). (a) Experimental results of LaCoO_3 single crystal. (b, c) Simulated spectra of ${}^1A_{1g}(O_h)$ ground state (b) without including and (c) including the saturation and the self-absorption effects. The scattering geometry of the calculation is identical to the angle used in the experiment on the LaCoO_3 single crystal ($\alpha + \beta = 140^\circ$; horizontally-polarized incident photons).

saturation and the self-absorption effects should be considered in a concentrated sample. By including the saturation and the self-absorption effects, the multiplied results show good agreement for the trends of the angular dependence except that the elastic peak is overestimated [Fig. 4(c)]. Although the spectra were distorted, the small energy shifts of the ${}^3T_{1g}$ excited states are still preserved theoretically. Unfortunately, better statistics and energy resolution are required to observe this tiny shift in the experiment.

For an isotropic ${}^1A_{1g}$ ground state, in general, no angular dependence in a dipole $2p3d$ transition ($2p$ XAS) is observed (Merz *et al.*, 2010). However, the effective dd transition operator W_{Qq} determines the $2p3d$ RIXS cross-section, where the intermediate state plays an important role. This transition operator can be quadruple-like (rank 2 transition) because of the combination of two dipole transitions (rank 1 transition). On the one hand, the incident absorption channel of RIXS excites the ground state to intermediate states which preserve a mixture of different symmetries. On the other hand, due to the spin-orbit coupling, the final excited state splits into different branches with a small energy difference. In combination, the effective transition preserves spin and orbit characteristics and the polarization weighting factor $T_{Qq}(\varepsilon_E, \varepsilon_I)$ provides the intensity of states as a function of geometry (van Veenendaal, 2006; Haverkort *et al.*, 2010). In order to confirm

this idea, 20 meV resolved $2p3d$ RIXS simulations were performed. Figs. 5(a) and 5(b) show the $2p3d$ RIXS spectra of three geometries with the scattering angle ($\alpha + \beta$) set to 90° . With a finer broadening, the energy splittings caused by spin-orbit coupling are better resolved [Figs. 5(a) and 5(b)]. The ${}^3T_{1g}$ states split into the E_g , T_{2g} , T_{1g} and A_{1g} states, where we have indicated the double-group labels in italic. In the case of vertically-polarized incident photons (V-polarization), the elements in the polarization tensor equally contribute in all geometries. Thus, no angular dependence is expected [*cf.* Fig. 5(b)]. In contrast, the horizontally-polarized incident beam (H-polarization) induces the polarization tensor to change as a function of rotation angle. Thus, the angular dependence is pronounced and depends on the spin and orbit characteristics of the initial and the final state. Figs. 5(c) and 5(d) present the angle-dependent behavior of different polarizations by plots of the RIXS cross-section probed at the maximum of the L_3 edge as a function of rotation angle. Here the E_g and T_{2g} groups of the ${}^3T_{1g}$ state are selected for comparison. We note that the broadening of the spectra in Fig. 4 has been increased due to the limiting experimental resolution. Hence the angular dependence reflects the intensity competition and energy shift.

One way to avoid the self-absorption effect is by reducing the sample thickness, so that the emission intensity is an energy-independent function of the rotation angle [*cf.* equa-

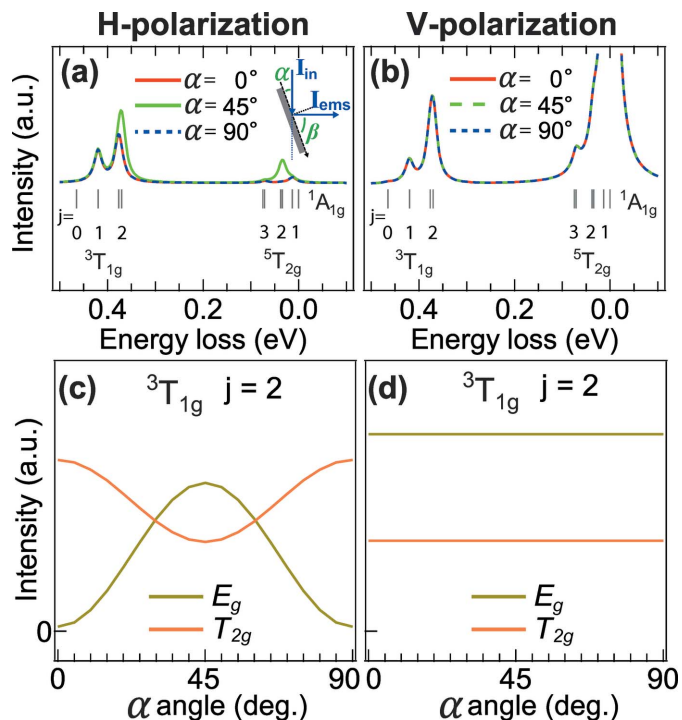


Figure 5
(a, b) $2p3d$ RIXS simulations of the ${}^1A_{1g}(O_h)$ ground state as a function of the sample rotation angle α with respect to (a) H-polarization and (b) V-polarization. Small broadening (20 meV) is used in the simulations. (c, d) $2p3d$ RIXS transition cross-section of the ${}^3T_{1g}$ excited state as a function of the rotation angle α with respect to (c) H-polarization and (d) V-polarization. Presented here are only the states with a total moment equal to two ($j = 2$). The scattering angle is now replaced by 90° .

tion (10)]. Once we normalize the spectra to the fluorescence feature, the intensity of the dd excitations can be represented properly. We examine the angle-dependent $2p3d$ RIXS of the 55 nm LaCoO_3 film grown on the SrTiO_3 substrate. This thickness is on the limit of the attenuation length of the $\text{Co } L_3$ edge (25–125 nm) but can still be considered to be free from self-absorption effects (see further arguments in Appendix A). The dd excitations are now less influenced by the self-absorption effect and are mainly determined by the polarization selectivity – see Fig. 6. Most of the angle-dependent features agree with the calculation of the ${}^5B_{2g}(\text{D}_{4h})$ ground state (gray arrows). As has been discussed, the ground state of the Co^{3+} ions in the $\text{LaCoO}_3/\text{SrTiO}_3$ film shows a mixture of the low-spin ${}^1A_{1g}(\text{O}_h)$ state and high-spin ${}^5B_{2g}(\text{D}_{4h})$ state (Wang *et al.*, 2019). Compared with the ${}^5B_{2g}(\text{D}_{4h})$ state, the angular dependence of RIXS is negligible for the ${}^1A_{1g}(\text{O}_h)$ state (Fig. 6). The angle-independent features of the ${}^1A_{1g}(\text{O}_h)$ state are indicated by black arrows, but are almost invisible compared with the ${}^5B_{2g}(\text{D}_{4h})$ ground state. Some discrepancies remain, for example the 1.3 eV feature indicated with the red arrow in the ${}^5B_{2g}(\text{D}_{4h})$ calculation is not evident in the experimental data. This could be because: (i) the mixture of the spin states suppresses the intensity of the 1.3 eV feature (Wang *et al.*, 2019); (ii) we assumed that the CoO_6 clusters are well aligned to the pseudo-cubic orientation (002) – experimentally, not all the CoO_6 clusters should be aligned exactly along the pseudo-cubic orientation; (iii) the discussions above do not take the trigonal symmetry reduction into account. The CoO_6 clusters are naturally aligned in a trigonal field for a relaxed LaCoO_3 crystal (the space group of the unit cell is $R\bar{3}c$). By including the trigonal distortion, the polarization selectivity might be different from the tetragonal distortion.

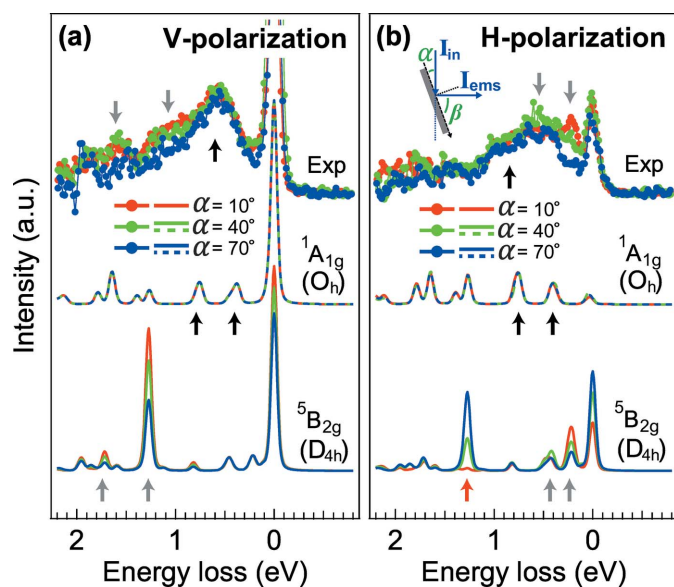


Figure 6
The $2p3d$ RIXS results of the 55 nm $\text{LaCoO}_3/\text{SrTiO}_3$ film compared with the ${}^1A_{1g}(\text{O}_h)$ and ${}^5B_{2g}(\text{D}_{4h})$ ground states. Both the (a) V- and (b) H-polarized are calculated and measured at a geometry for a scattering angle of 90° .

5. Conclusions

We have presented the angular dependence of $2p3d$ RIXS analyzed with the scattering cross-section including saturation and self-absorption effects. The angle-dependent spectra are a better probe of the symmetry type than using only the difference between two orthogonal polarizations, due to the angular relation between the ground/excited states symmetry and the polarization tensor. A remarkable consequence is that even the isotropic low-spin ${}^1A_{1g}(\text{O}_h)$ ground state shows angle-dependent $2p3d$ RIXS spectra, despite the absence of angular dependence in the $2p$ XAS spectra (Merz *et al.*, 2010; Wang *et al.*, 2019). Unfortunately, the high Co concentration in the LaCoO_3 single crystal distorts the RIXS spectra due to the saturation and self-absorption effects which limits the distinguishability. By applying a model to consider these effects, the trends are explained as a function of both the energy and the rotation angle. In contrast, for the $\text{LaCoO}_3/\text{SrTiO}_3$ film, the self-absorption effect is small. Thus the $\text{LaCoO}_3/\text{SrTiO}_3$ film shows better agreement with the angular trend although some features are not reproduced well. The possible reason for this mismatch could be a mixture of ground states, non-perfect empirical parameters and/or reduced symmetry.

APPENDIX A

Estimation of the attenuation length of the elements at the $\text{Co } L_3$ edge (~ 780 eV)

In the main text, we use the relative relation of the absorption factor (μ) to describe the trends of the saturation and self-absorption effects. Here we provide the experimental quantities of different elements in the LaCoO_3 to estimate the following questions: (a) What is the maximum attenuation length of the $\text{Co } L_3$ edge? (b) What is the critical film thickness in order to claim the absence of the self-absorption effect? (c) What is the reasonable weighting for μ_B ?

According to the tabulated data (Henke *et al.*, 1993), the attenuation length at 780 eV for the La, O and Co elements in the LaCoO_3 ($\rho = 7.25 \text{ g cm}^{-3}$) are ~ 950 , ~ 810 and ~ 380 nm, respectively. The values show that the attenuation length of Co is much longer than our film thickness (55 nm), which leads to the consequence that our film can be self-absorption free.

However, the attenuation length values at the absorption edge are likely overestimated using Henke's table. For cobalt metal ($\rho = 8.9 \text{ g cm}^{-3}$), the estimated attenuation length is ~ 75 nm but the experimental results indicate that the attenuation length was ~ 25 nm at the peak maximum (Chen *et al.*, 1995). By considering that the mass weight of Co is about 25% in the LaCoO_3 ($\rho_{\text{Co}} = 1.8 \text{ g cm}^{-3}$), the attenuation length of the $\text{Co } L_3$ edge peak maximum is ~ 125 nm (five times larger). This value is still larger than our film thickness of ~ 55 nm.

On the other hand, the self-absorption effect on the RIXS profile will be dependent on the intrinsic lifetime broadening. If we set a lifetime broadening of 300 meV, the selected energy at a few hundred meV away from maximum of the L_3 resonance peak has an attenuation length a few times longer. This

implies that we can treat the 55 nm LaCoO₃ film as being free from self-absorption effect at the orbital excitations (>200 meV). However, we remark that minor self-absorption effects could be visible for the elastic and low-loss features (<150 meV).

Here we estimate the background absorption. The weighting of μ is proportional to the inverse of the attenuation length. It gives values of 2–10%, 3–12% and 95–78% with respect to elements La, O and Co (attenuation lengths are 950, 810 and 25–125 nm), respectively. The background absorption factor (μ_B) is the off-resonant contribution from the other elements (except Co) and is estimated to be about 5–22%. We set μ_B as $\sim 5\%$ of μ_{\max} in our model.

APPENDIX B RIXS spectra normalization

Fig. 7 presents our treatment on the RIXS spectrum of the LaCoO₃/SrTiO₃ film. The blue peaks are the *dd* excitations which were fitted by Gaussian functions, grouped with the elastic peak at 0 eV, low-energy peaks at ~ 0.1 – 0.2 eV and the other excitations at about 0.4, 0.8, 1.3, 1.5 and 2.0 eV. The broadening is increased from 0.1 to 0.4 eV (FWHM) with the increase of the energy loss.

In order to compare the calculation with the experimental results, we normalized the spectra to the summed area of the charge transfer/fluorescence features. These features (>2 eV) are expected to be self-absorption free according to our discussion. We use five Gaussian functions to simulate the experimental fluorescence profile (gray area in Fig. 7). This fluorescence profile was used for the normalization procedure. After the spectra were normalized, the fluorescence profile was subtracted from the normalized spectra.

Acknowledgements

The authors thank the technical staff of Taiwan Light Source for their help with the RIXS measurements. We thank David Ellis for the fruitful discussion.

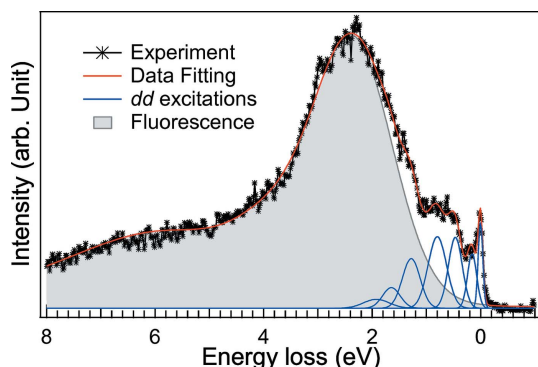


Figure 7
Fitting treatment of the RIXS spectra for LaCoO₃/SrTiO₃ film. Blue peaks are the Gaussian fitting profiles of *dd* excitation features. The gray area is the fitting profile for the fluorescence feature.

Funding information

The experiments were supported by ERC advanced grant (grant agreement No. 340279-XRAYonACTIVE). DJH was supported by the Ministry of Science and Technology of Taiwan under Grant No. 106-2112-M-213-008-MY3. KT was financially supported by the MEXT and JSPS KAKENHI (JP17H06137, JP15H03692, JP18K03503). CHD was supported by the MOST through the grant 105-2119-M-032-002-MY2. JG and GK acknowledge The Netherlands Organization for Scientific Research (NWO) and the NWO/FOM programme DESCO (VP149).

References

Achkar, A. J., Regier, T. Z., Wadati, H., Kim, Y.-J., Zhang, H. & Hawthorn, D. G. (2011). *Phys. Rev. B*, **83**, 081106.
 Chabot-Couture, G., Hancock, J. N., Mang, P. K., Casa, D. M., Gog, T. & Greven, M. (2010). *Phys. Rev. B*, **82**, 035113.
 Chakarian, V., Idzerda, Y. U. & Chen, C. T. (1998). *Phys. Rev. B*, **57**, 5312–5315.
 Chen, C. T., Idzerda, Y. U., Lin, H.-J., Smith, N. V., Meigs, G., Chaban, E., Ho, G. H., Pellegrin, E. & Sette, F. (1995). *Phys. Rev. Lett.* **75**, 152–155.
 Dallera, C., Braicovich, L., Ghiringhelli, G., van Veenendaal, M. A., Goedkoop, J. B. & Brookes, N. B. (1997). *Phys. Rev. B*, **56**, 1279–1283.
 Eisebitt, S., Böske, T., Rubensson, J.-E. & Eberhardt, W. (1993). *Phys. Rev. B*, **47**, 14103–14109.
 Groot, F. (2005). *Coord. Chem. Rev.* **249**, 31–63.
 Groot, F. M. F. de, Arrio, M., Sainctavit, P., Cartier, C. & Chen, C. (1994). *Solid State Commun.* **92**, 991–995.
 Haverkort, M. W. (2010). *Phys. Rev. Lett.* **105**, 167404.
 Haverkort, M. W., Hollmann, N., Krug, I. P. & Tanaka, A. (2010). *Phys. Rev. B*, **82**, 094403.
 Haverkort, M. W., Zwierzycki, M. & Andersen, O. K. (2012). *Phys. Rev. B*, **85**, 165113.
 Henke, B. L., Gullikson, E. M. & Davis, J. C. (1993). *At. Data Nucl. Data Tables*, **54**, 181–342.
 Jaklevic, J., Kirby, J. A., Klein, M. P., Robertson, A. S., Brown, G. S. & Eisenberger, P. (1977). *Solid State Commun.* **23**, 679–682.
 Juhin, A., Brouder, C. & de Groot, F. (2014). *Cent. Eur. J. Phys.* **12**, 323–340.
 Kramers, H. A. & Heisenberg, W. (1925). *Z. Phys.* **31**, 681–708.
 Lai, C. H., Fung, H. S., Wu, W. B., Huang, H. Y., Fu, H. W., Lin, S. W., Huang, S. W., Chiu, C. C., Wang, D. J., Huang, L. J., Tseng, T. C., Chung, S. C., Chen, C. T. & Huang, D. J. (2014). *J. Synchrotron Rad.* **21**, 325–332.
 Liu, B., Glass, E. N., Wang, R., Cui, Y., Harada, Y., Huang, D. J., Schuppler, S., Hill, C. L. & de Groot, F. M. F. (2018). *Phys. Chem. Chem. Phys.* **20**, 4554–4562.
 Luo, J., Trammell, G. T. & Hannon, J. P. (1993). *Phys. Rev. Lett.* **71**, 287–290.
 Merz, M., Nagel, P., Pinta, C., Samartsev, A., Löhneysen, H. v., Wissinger, M., Uebe, S., Assmann, A., Fuchs, D. & Schuppler, S. (2010). *Phys. Rev. B*, **82**, 174416.
 Minola, M., Dellea, G., Gretarsson, H., Peng, Y. Y., Lu, Y., Porras, J., Loew, T., Yakhov, F., Brookes, N. B., Huang, Y. B., Pellicciari, J., Schmitt, T., Ghiringhelli, G., Keimer, B., Braicovich, L. & Le Tacon, M. (2015). *Phys. Rev. Lett.* **114**, 217003–217008.
 Moretti Sala, M., Bisogni, V., Aruta, C., Balestrino, G., Berger, H., Brookes, N. B., Luca, G. M., Di Castro, D., Grioni, M., Guarise, M., Medaglia, P. G., Miletto Granozio, F., Minola, M., Perna, P., Radovic, M., Salluzzo, M., Schmitt, T., Zhou, K. J., Braicovich, L. & Ghiringhelli, G. (2011). *New J. Phys.* **13**, 043026.

- Nakajima, R., Stöhr, J. & Idzerda, Y. U. (1999). *Phys. Rev. B*, **59**, 6421–6429.
- Schooneveld, M. M. van, Kurian, R., Juhin, A., Zhou, K., Schlappa, J., Strocov, V. N., Schmitt, T. & de Groot, F. M. F. (2012). *J. Phys. Chem. C*, **116**, 15218–15230.
- Tomiyasu, K., Okamoto, J., Huang, H. Y., Chen, Z. Y., Sinaga, E. P., Wu, W. B., Chu, Y. Y., Singh, A., Wang, R.-P., de Groot, F. M. F., Chainani, A., Ishihara, S., Chen, C. T. & Huang, D. J. (2017). *Phys. Rev. Lett.* **119**, 196402.
- Tröger, L., Arvanitis, D., Baberschke, K., Michaelis, H., Grimm, U. & Zschech, E. (1992). *Phys. Rev. B*, **46**, 3283–3289.
- Veenendaal, M. van (2006). *Phys. Rev. Lett.* **96**, 117404.
- Wang, R.-P., Geessinck, J., Elnaggar, H., Birkhölzer, Y. A., Tomiyasu, K., Okamoto, J., Liu, B., Du, C.-H., Huang, D.-J., Koster, G. & de Groot, F. M. F. (2019). *Phys. Rev. B*, **100**, 165148.
- Zschech, E., Tröger, L., Arvanitis, D., Michaelis, H., Grimm, U. & Baberschke, K. (1992). *Solid State Commun.* **82**, 1–5.